Engineering Fracture Mechanics 98 (2013) 185–199

Contents lists available at SciVerse ScienceDirect

Engineering Fracture Mechanics

journal homepage: www.elsevier.com/locate/engfracmech

Measurement of crack-tip and punch-tip transient deformations and stress intensity factors using Digital Gradient Sensing technique

Chandru Periasamy, Hareesh V. Tippur *

Department of Mechanical Engineering, Auburn University, AL 36849, United States

ARTICLE INFO

Article history:
Received 17 May 2012
Received in revised form 4 September 2012
Accepted 15 September 2012

Keywords:
Experimental fracture mechanics
Optical measurements
High speed photography
Speckle imaging
Elasto-optic effect
Stress gradients
Transparent materials
Dynamic crack growth
Impact loading
Stress intensity factors

ABSTRACT

The optical method of Digital Gradient Sensing (DGS) is extended to the study of fracture mechanics and impact mechanics problems. DGS is based on the elasto-optic effect exhibited by transparent materials subjected to non-uniform state of stress causing the angular deflection of light rays propagating through the material. Under plane stress conditions, the deflections of light rays can be related to two orthogonal in-plane stress gradients. In this paper, the principle of the method is presented first, followed by crack and punch experiments on PMMA plates for quantifying stress gradients near stress risers. The crack-tip stress intensity factors under both quasi-static and dynamic loading conditions are extracted from DGS measurements and are in good agreement with analytical and finite element results. The problem of a square-punch impacting the edge of a PMMA sheet is also studied using the new method by exploiting punch-tip–crack-tip analogy. The dynamic punch-tip stress intensity factors are extracted from the optical measurements and are again in good agreement with the ones from a complementary finite element analysis of the problem.

1. Introduction

Understanding the fracture behavior of materials is vital to the design of critical structures. Its implications are even greater for materials used in transparent armor [1], helmet visors, aircraft canopies, etc., for shielding personnel and/or sensitive equipment while providing adequate optical transparency. Other more common situations include structural window materials, impact resistant transparent enclosures and composites. Wright et al. [2] have reported on ballistic testing of thick and thin polycarbonate plates in which different mechanisms of dynamic failure including elastic dishing, petalling, deep penetration, cone cracking and plugging have been identified. Numerous studies exist on dynamic fracture of transparent polymers for understanding either the material behavior or for validating fracture mechanics theories by utilizing their optical transparency [3–7]. In other works, fracture mechanics of glass and other transparent ceramics have been studied either in the monolithic form or layered form [8–11] for their crack deflection, crack arrest and fragmentation responses.

In fracture mechanics studies, experimental procedures that employ full-field measurement techniques are preferred, as they offer abundant qualitative as well as quantitative data for analysis when compared to point-wise methods. Among them photoelasticity [12,13], moiré interferometry [14], caustics [15,16] and coherent gradient sensing (CGS) [17,18] have all been used to study dynamic crack growth problems. However, since these techniques use light as the sensing signal, they also have certain restrictions – need for specimen birefringence, extensive surface preparation and/or sophisticated coherent optics, to name a few. In recent times, digital image correlation (DIC) techniques have become increasingly popular as they re-

* Corresponding author. Tel.: +1 334 844 3327.
E-mail address: tippuhv@auburn.edu (H.V. Tippur).

0013-7944/$ - see front matter © 2012 Elsevier Ltd. All rights reserved.
http://dx.doi.org/10.1016/j.engfracmech.2012.09.011

Nomenclature

$\hat{d}$	unit propagation vector
$\hat{i},\hat{j},\hat{k}$	unit vectors in *x*-, *y*- and *z*-directions
$\alpha_x,\alpha_y,\alpha_z$	direction cosines
δS	optical path change
n	refractive index
B	thickness
σ	normal stress
ε	normal strain
E	elastic modulus
ν	Poisson's ratio
C_σ	elasto-optic constant
ϕ_x, ϕ_y	angular components
θ_x, θ_y	solid angles
δ_x, δ_y	displacement components
Δ	target distance
r, θ	crack tip polar coordinates
a	crack length
W	uncracked ligament length
K_I	mode-I stress intensity factor
K_p	punch tip stress intensity factor
C_L, C_s	longitudinal and shear wave speeds
C	crack speed
u_2	crack opening displacement
t	time
V	particle velocity
ρ	density
A	area

quire ordinary white light illumination, relatively simple optics, digital electronics and little/no surface preparation [19]. With the recent introduction of ultra high-speed digital photography (>100,000 frames per sec) capable of high temporal *and* spatial resolutions, DIC is becoming a method of choice to study transient fracture problems [20–22] as well. As an extension of DIC based methods, the authors have recently introduced a full-field optical technique called Digital Gradient Sensing (DGS) [23] that employs 2D DIC method for quantifying elasto-optic effects in transparent materials. They have also been able to link the optical measurements to two orthogonal in-plane stress gradients under plane stress conditions. The method is shown to be particularly useful in the study of stress concentration problems. The focus of the current work is on demonstrating the feasibility of DGS for measuring crack-tip stress gradients and extraction of stress intensity factors.

In the following, the experimental setup, working principle and governing equations for the DGS method are discussed first. Next, the implementation of DGS method to quasi-static and dynamic crack problems is detailed. The extraction of mode-I stress intensity factors and comparisons of the measured angular deflections with analytical and numerical solutions for quasi-static and dynamic cases, respectively, follow. Finally, the problem of a square punch impacting the edge of a planar sheet is reported in view of its analogous features to a double edged crack subjected to a far-field compressive load perpendicular to the crack faces. This analogy permits the use of mode-I crack-tip fields to extract punch-tip stress intensity factors which have been compared with the ones based on an elasto-dynamic finite element simulation of the problem.

2. Experimental setup

A schematic of the experimental setup for Digital Gradient Sensing (DGS) method is shown in Fig. 1. In view of its relative novelty [23] to the fracture mechanics community, the experimental details and the working principle of DGS are detailed in the following for studying fracture and contact mechanics problems. It consists of a uniformly illuminated speckle target, an optically transparent specimen with an edge crack and a digital camera. The speckle target is a planar surface coated with a stochastic black and white pattern produced by spraying fine mists of black and white paints. The transparent specimen to be tested is placed in front of and parallel to the target plane at a known distance Δ (=distance between the mid-plane of the specimen and the target plane). A camera fitted with a long focal length lens is placed behind the specimen at a sufficiently large distance L and focused on the target through the specimen in the region of interest. The target is illuminated using two broadband white light sources. The illumination sources are situated sufficiently far away from the specimen to minimize thermal currents from distorting the speckle images and/or heating the specimen during the experiment. The digital camera

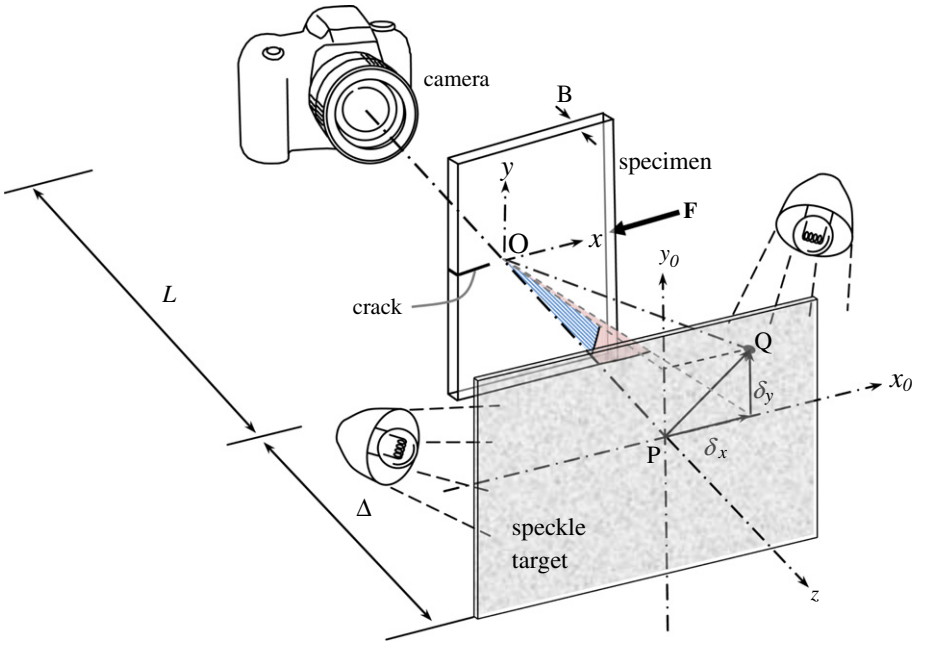

Fig. 1. Schematic of the experimental set up for the Digital Gradient Sensing (DGS) method to determine planar stress gradients near a crack tip.

settings and lens parameters are selected such that the aperture is sufficiently small for achieving a good focus of speckles on the target whilst preserving the salient features of the specimen plane (say, crack/flaw, specimen edges, etc.) discernible in the recorded image for easy post processing of data.

3. Working principle and governing equations

Consider a planar transparent specimen of thickness B and refractive index n in its reference state. Let the in-plane coordinates of the specimen and target planes be (x,y) and (x_0,y_0), respectively, and the optical axis of the setup coincide with the z-axis (see Fig. 1). When speckles on the target plate are photographed normally through the transparent specimen, a generic point P on the target plane, corresponding to point O on the specimen (object) plane, is recorded by the camera in the reference state. When subjected to mechanical load, both refractive index and thickness changes occur throughout the specimen depending on the local state of stress. A combination of these changes causes light rays to deflect as shown in Fig. 1. That is, the light ray OP recorded in the reference/undeformed state now corresponds to OQ after the specimen deforms. By quantifying PQ and knowing the spatial separation Δ between the mid-plane of the specimen and the target plane, the angular deflection of the light ray relative to the optical axis can be determined.

Let $\hat{i},\hat{j}$, and $\hat{k}$ denote unit vectors relative to the Cartesian coordinates defined with point O as the origin. In the reference state, the unit vector $\hat{k}$ coincides with OP bringing point P(x_0,y_0) to focus when imaged by the camera via point O(x,y). Upon deformation, the optical path is locally perturbed, bringing a neighboring point Q$(x_0+\delta_x, y_0+\delta_y)$ to the camera's focus, where δ_x and δ_y denote components of PQ in the x- and y-directions. Let the unit vector corresponding to the perturbed optical path be,

$$\hat{d} = \alpha_x\hat{i} + \alpha_y\hat{j} + \alpha_z\hat{k}, \tag{1}$$

where α_x, α_y and α_z are the direction cosines of $\hat{d}$, and components of the angular deflection be ϕ_x and ϕ_y in the x–z and y–z planes, respectively, as shown in Fig. 2.

The optical path change, δS, due to the deformation of the specimen can be expressed as [17],

$$\delta S(x,y) = 2B(n-1)\int_0^{1/2} \varepsilon_{zz}\, d(z/B) + 2B\int_0^{1/2} \delta n\, d(z/B) \tag{2}$$

The two terms in the above equation represent the contribution of normal strain in the thickness direction, ε_{zz}, and the change in the refractive index, δn, to the overall optical path change, respectively. The refractive index change caused by the local stress state in the specimen, is given by the well known Maxwell relationship [24],

$$\delta n(x,y) = D_1(\sigma_{xx} + \sigma_{yy} + \sigma_{zz}) \tag{3}$$

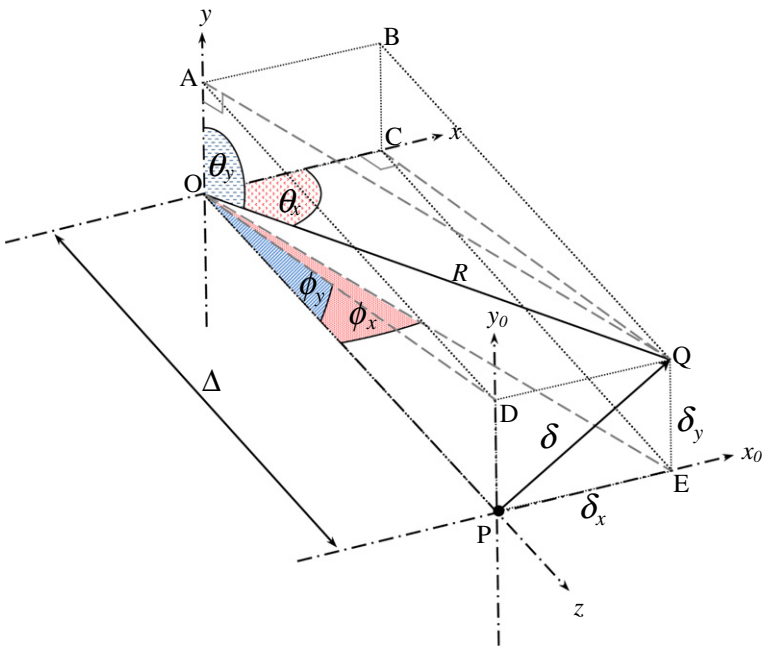

Fig. 2. Schematic representing measured quantities and their relationship to other geometric parameters used in DGS.

where D_1 is the stress-optic constant. Using the generalized Hooke's law for an isotropic, linear elastic solid, the normal strain component, $\varepsilon_{zz}\left(=\frac{1}{E}[\sigma_{zz}-\nu(\sigma_{xx}+\sigma_{yy})]\right)$ can be related to the normal stresses. That is, Eq. (2) can be written as,

$$\delta S = 2B\left(D_1 - \frac{\upsilon}{E}(n-1)\right)\int_0^{1/2}\left\{(\sigma_{xx}+\sigma_{yy})\left[1+D_2\left(\frac{\sigma_{zz}}{\upsilon(\sigma_{xx}+\sigma_{yy})}\right)\right]\right\}d(z/B) \tag{4}$$

where $D_2 = [\nu D_1 + \nu(n-1)/E]/[D_1 - \nu(n-1)/E]$, E is the elastic modulus and ν is the Poisson's ratio for the specimen. In the above equation, the term $D_2\left(\frac{\sigma_{zz}}{\upsilon(\sigma_{xx}+\sigma_{yy})}\right)$ represents the degree of plane strain, which can be neglected when plane stress assumptions are reasonable. Thus, for plane stress conditions, Eq. (4) reduces to,

$$\delta S(x,y) = C_\sigma B(\sigma_{xx}+\sigma_{yy}) \tag{5}$$

where $C_\sigma = D_1 - (\upsilon/E)(n-1)$ is the elasto-optic constant of the specimen. From the above equation, the propagation vector can also be represented as,

$$\hat{d} \approx \frac{\partial(\delta S)}{\partial x}\hat{i} + \frac{\partial(\delta S)}{\partial y}\hat{j} + \hat{k} \tag{6}$$

for small rates of change of δ_x with respect to the x- and y-axes. From Eqs. (1), (5), and (6), it is evident that, for small angular deflections, the direction cosines α_x and α_y are related to in plane stress gradients as,

$$\alpha_{x:y} = \frac{\partial(\delta S)}{\partial(x:y)} = C_\sigma B\frac{\partial(\sigma_{xx}+\sigma_{yy})}{\partial(x:y)} \tag{7}$$

A geometric analysis of the perturbed ray OQ shows the relationship between the direction cosines α_x and α_y and angular deflection components ϕ_x and ϕ_y, respectively. Referring to Fig. 2, the perturbed ray makes solid angles θ_x and θ_y with the x- and y-axes. The angular deflections ϕ_x, ϕ_y as defined earlier are also shown in Fig. 2. With reference to the planes defined by points OQC and OPE,

$$\cos\theta_{x:y} = \frac{\delta_{x:y}}{R}, \tag{8}$$

respectively, where $R\left(=\sqrt{\Delta^2+\delta_x^2+\delta_y^2}\right)$ is the distance between O and Q. From the above, the expressions for the angular deflection components can be obtained as,

$$\tan\phi_{x:y} = \frac{R}{\Delta}\cos\theta_{x:y} = \sqrt{1+\frac{\delta_x^2+\delta_y^2}{\Delta^2}}\cos\theta_{x:y}. \tag{9}$$

It can be noted from Eq. (9) that for small angular deflections (or, $\delta_x, \delta_y \ll \Delta$), the expressions reduce to $\phi_{x:y} \approx \cos\theta_{x:y} = \alpha_{x:y}$. Thus, for the case of small angular deflections of light rays, the governing equations for the method reduce to,

$$\phi_{x:y} \approx \frac{\delta_{x:y}}{\Delta} \approx \alpha_{x:y} = C_\sigma B \frac{\partial(\sigma_{xx} + \sigma_{yy})}{\partial(x:y)}, \tag{10}$$

using which stress gradients can be obtained from angular deflections. Thus by photographing speckles on the target plane through the specimen before and after the application of load, the reference and deformed speckle patterns can be digitally acquired. Subsequently, 2D digital image correlation of the two acquired images yields full-field information regarding displacements δ_x and δ_y. Knowing the distance Δ between the specimen and target planes, angles ϕ_x and ϕ_y can be evaluated.

4. Quasi-static crack problem

4.1. Experimental setup

Using the method described above, a quasi-static symmetric 3-point bend experiment on an edge cracked specimen was performed. A photograph of the experimental setup is shown in Fig. 3. A transparent PMMA specimen of dimensions $220 \times 62.5 \times 9.2$ mm^3, with an initial crack length of 12 mm was used as the test specimen. (PMMA was chosen since its elasto-optical constant C_σ is documented in the literature [25].) An Instron 4465 universal testing machine was used to load the sample resting on two anvils (span 210 mm) in displacement controlled mode (cross-head speed = 0.005 mm/s). A target plate, painted with black and white speckle pattern, was placed at a distance of (Δ =)29.9 mm behind the mid-plane of the specimen. Multiple reference points were marked on the target to help relate the image dimensions to the actual dimensions. A Nikon D100 digital SLR camera with a 28–300 mm focal length lens was placed in-front of the specimen at approximately one meter distance. The camera also used an adjustable extension tube to achieve good focus of speckles on the target plane. Further, a relatively small aperture (F$^{\#}$ setting of 11) was selected to achieve a good depth of focus to resolve specimen features while maintaining target plane focus. Before loading, a reference image was recorded using a camera resolution of 1504×1000 pixels (one pixel covered 43.6 μm on the target). Subsequently, speckle images were captured in the

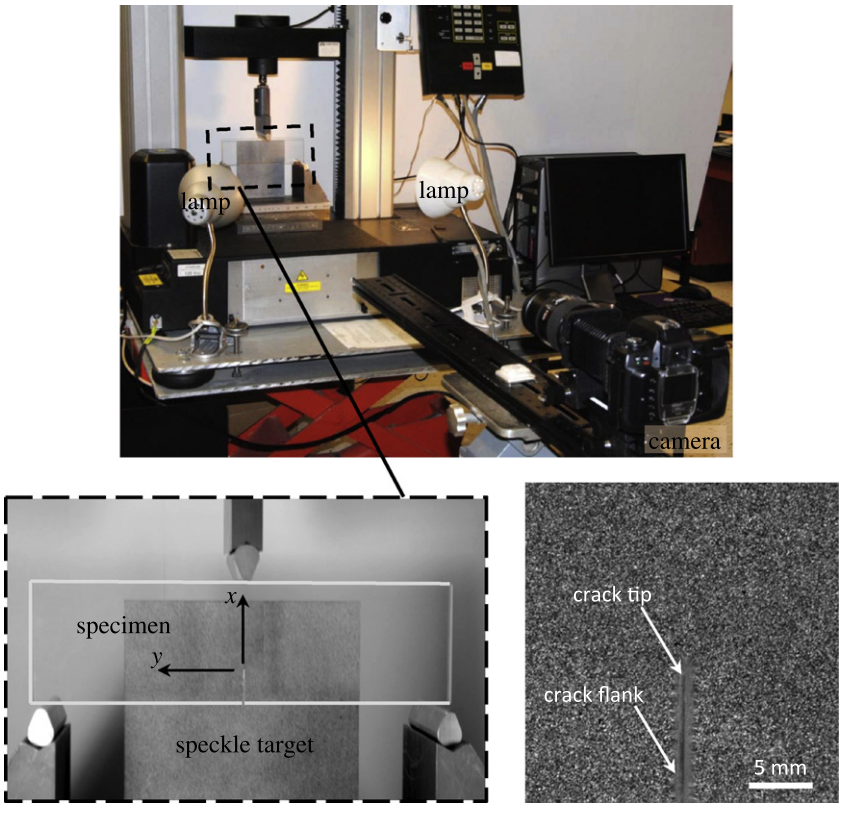

Fig. 3. Experimental setup used to measure angular deflections of light rays caused by a mode-I crack in a planar transparent 3-point bend specimen subjected to quasi-static loading. A sample speckle recording corresponding to a static load of 624 N is shown as an inset.

deformed state once every 5 s during loading using time lapse photography. As the crack-tip vicinity suffered deformation, light rays passing through the specimen were deflected by the local non-uniform state of stress distorting the speckle images relative to the reference state. The images corresponding to the deformed state along with the one from the reference state were then used to extract the angular deflection fields (ϕ_x and ϕ_y) using 2D digital image correlation using ARAMIS image analysis software. During the analysis, the images were segmented into 15×15 pixel non-overlapping sub-images. This yielded an array of 99×65 data points to analyze.

Fig. 4 shows the resulting contours of ϕ_x and ϕ_y for three representative load levels in a square region around the crack-tip. The assignment of contour levels requires using the boundary conditions [26] of the problem on hand. For example, in the mode-I crack problem, boundary conditions such as symmetric ϕ_x and asymmetric ϕ_y about the x-axis, vanishing stress gradients far away from the crack-tip and stress free surfaces along the edges behind the crack are all considered while assigning the contour levels. It should be noted that the contour lines adjacent to the crack faces in Fig. 4 appear smeared due to unavoidable edge effects. Additionally, diffraction effects also contribute to the loss of information along a narrow band adjacent to the two crack faces.

It should also be noted that the orthogonal angular deflection contours shown in Fig. 4 closely resemble the ones obtained using the method of transmission mode CGS (see Fig. 7 in Ref. [4]). Furthermore, the angular deflection gradients in the x- and y-directions in Fig. 4 were produced using a single image/recording whereas the orientation of the optical shearing device (a pair of linear gratings) had to be changed by 90° in two separate experiments to achieve the results shown in Ref. [17] using CGS.

4.2. Extraction of K_I

From Williams' asymptotic stress field expansion for mode-I cracks, the expressions for angular deflections (or in-plane gradients of stresses) can be expressed as [17],

$$\phi_{x:y} = C_\sigma B \frac{\partial(\sigma_{xx} + \sigma_{yy})}{\partial(x:y)} = C_\sigma B \sum_{N=1}^{\infty} A_N \left(\frac{N}{2} - 1\right) r^{\left(\frac{N}{2}-2\right)} \begin{matrix}\cos \\ \sin\end{matrix} \left(\frac{N}{2} - 2\right)\theta, \tag{11}$$

where $C_\sigma \approx -0.9 \times 10^{-10}$ m^2/N is the elasto-optic constant of PMMA [25], B = 9.2 mm is the thickness of the specimen, (r, θ) are the crack-tip polar coordinates and $A_1 = K_I \sqrt{\frac{2}{\pi}}$ with K_I being the mode-I stress intensity factor. In the above equations, if K–dominance is assumed (or, terms corresponding to $N \geqslant 3$ in Eq. (11) are neglected), we get

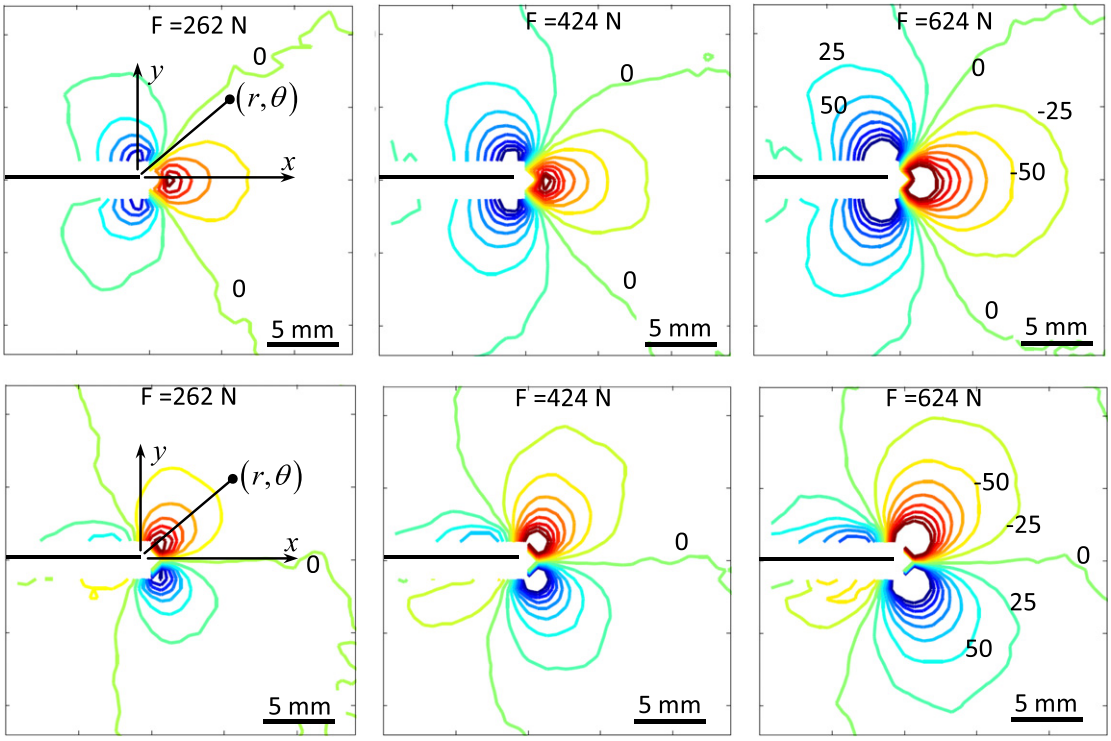

Fig. 4. Experimentally determined angular deflection (or, stress gradient) [ϕ_x (row 1) and ϕ_y (row 2)] contours near crack tip for different load levels. Contour interval is 25×10^{-5} radian.

$$\phi_{x,y} \approx C_\sigma B\left[\left(-\frac{A_1}{2}\right) r^{\left(-\frac{3}{2}\right)} \begin{matrix}\cos \\ \sin\end{matrix}\left(-\frac{3\theta}{2}\right)\right]. \tag{12}$$

The above angular deflection field equations were used to obtain the mode-I stress intensity factor (K_I) using an overdeterministic regression analysis of the measured data. Discrete angular deflection values around the crack-tip in the region $0.3 \leqslant r/B \leqslant 1.6$ and an angular extent ($-150° \leqslant \theta \leqslant +150°$) were used in the regression analysis. This ensured that data close to the crack-tip where triaxial effects are dominant are excluded from the regression analysis [17]. (Indirectly this helps in dealing with any uncertainty in the crack-tip location due to the edge effects introduced by the image correlation operation.) The upper bound ($r/B \sim 1.6$) of the radial extent makes sure that only those data points rich in the dominant mode I crack-tip field are included in the analysis. The results thus obtained are plotted in Fig. 5 for different load levels. The error bars shown in the graph correspond to stress intensity factors obtained by using different subsets of the ($0.3 \leqslant r/B \leqslant 1.6$) range. For comparison, the crack-tip stress intensity factors for different load levels, calculated using a result,

$$K_I = \frac{F \cdot S}{B \cdot W^{\frac{3}{2}}} \cdot \frac{3\left(\frac{a}{W}\right)^{\frac{1}{2}}\left[1.99 - \frac{a}{W}\left(1 - \frac{a}{W}\right)\{2.15 - 3.93\left(\frac{a}{W}\right) + 2.7\left(\frac{a}{W}\right)^2\}\right]}{2\left(1 + 2\frac{a}{W}\right)\left(1 - \frac{a}{W}\right)^{\frac{3}{2}}} \tag{13}$$

based on the boundary collocation method [27] are also presented in Fig. 5. In the above equation, F is the applied load, S is the distance between the supports, a is the initial crack length, and W is the specimen width. The stress intensity factors thus

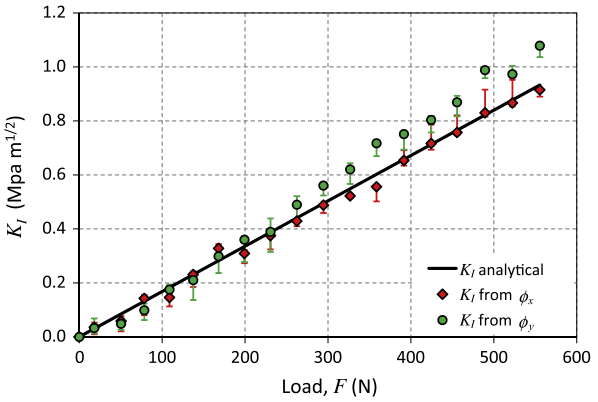

Fig. 5. Experimentally determined stress intensity factors from measured angular deflections near a mode-I static 3-point-bend crack problem for different applied load levels. The solid line represents the corresponding analytical values.

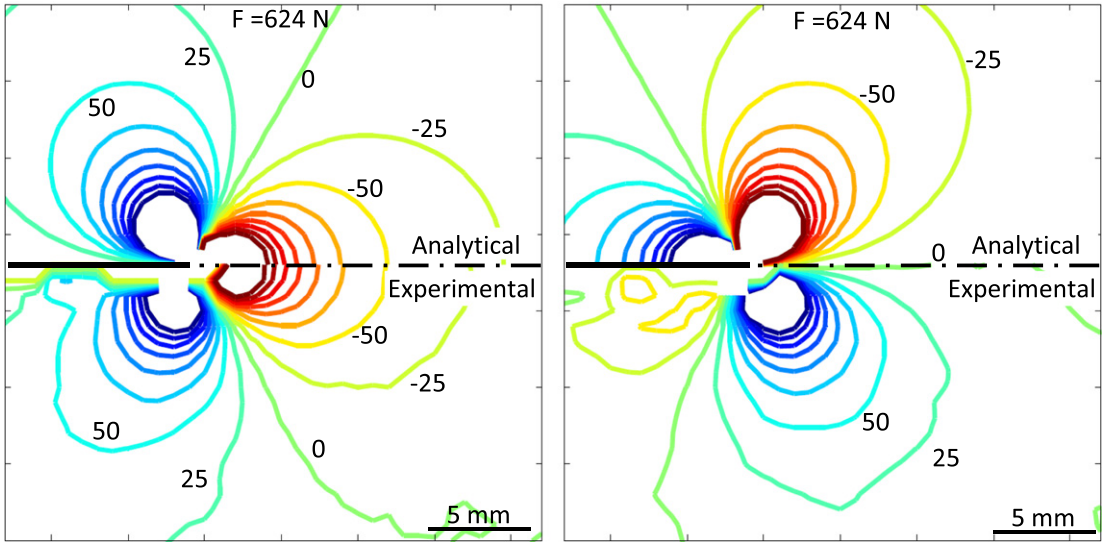

Fig. 6. Comparison of experimental and analytical ϕ_x (left) and ϕ_y (right) contours near the mode-I crack tip corresponding to a load of 624 N. Contours are plotted every 25×10^{-5} radian.

obtained were in turn used in Eq. (12) to obtain the analytical ϕ_x and ϕ_y contours. Fig. 6 shows a comparison of the experimental and analytical angular deflection contours for a representative load level of $F = 624$ N. Evidently the agreement between the analytical and experimental contour lines is rather good.

5. Dynamic crack problem

5.1. Experimental setup

The dynamic fracture experiments were performed on edge cracked PMMA samples using a drop-tower facility and high-speed photography. The photograph of the experimental setup used is shown in Fig. 7. The specimen was a $130 \times 51 \times 8.9$ mm^3 transparent PMMA sheet with an initial crack of length 12 mm. The specimen was placed on two instrumented anvils of the drop-tower, symmetrically about the crack line and the plunger (hemispherical impact head), as shown in Fig. 7. The speckle target was placed at a distance of $\Delta = 29.8$ mm from the mid-plane of the specimen. A Cordin model 550 ultra high-speed digital camera equipped with 32 CCD sensors (1000×1000 pixels) and a five-facet rotating mirror, two high-energy flash lamps and a delay generator was used to record the real time speckle images during stress wave loading. A computer connected to the camera was used to control the experimental parameters such as trigger delay, flash duration, framing rate and image storage. Prior to impact loading, a set of 32 images, one for each of the 32 CCD sensors of the high-speed camera, was captured at 200,000 frames per second. Then, the plunger, initially held at a predetermined height was launched to impact the mid-plane of the specimen at ~4.5 m/s. The propagating compressive stress waves upon reflection from the free edges behind the crack-tip load and initiate the crack-tip. When the plunger came in contact with a copper tape adhered to the top edge of the specimen, an external circuit was closed triggering the flash lamps and the high-speed camera previously brought to speed to record at 200,000 frames per second. Thus a second set of 32 images were recorded during the impact/fracture event. These latter set of images correspond to distorted speckle patterns as the deformation in the specimen cause the light rays passing through it to deflect according to the instantaneous local stress field. The 32 deformed–undeformed image pairs corresponding to the 32 CCD sensors were then correlated using 2D DIC method to obtain the in-plane displacement fields, δ_x and δ_y, in the region of interest near the crack-tip. As in the static experiments, a facet/sub-image size of 15×15 pixels (1 pixel = 32 μm on the target plane) without any overlap was used during image analyses for extracting displacement components along and normal to the crack direction. The displacement fields were then used to compute the angular deflections fields (ϕ_x and ϕ_y) as described earlier.

A few representative results are shown in Fig. 8. In Fig. 8, the first two columns correspond to pre crack initiation period, and the third to the post crack initiation period. It is obvious from the contour plots that the crack has propagated in a self-similar fashion, without any kink. The contour interval in Fig. 8 was chosen to be 50×10^{-5} radian which is an order of mag-

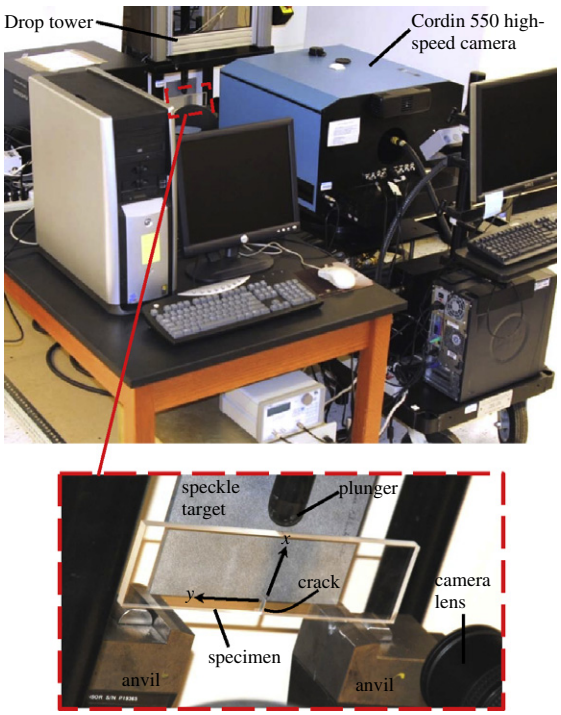

Fig. 7. Dynamic mode-I fracture experimental setup.

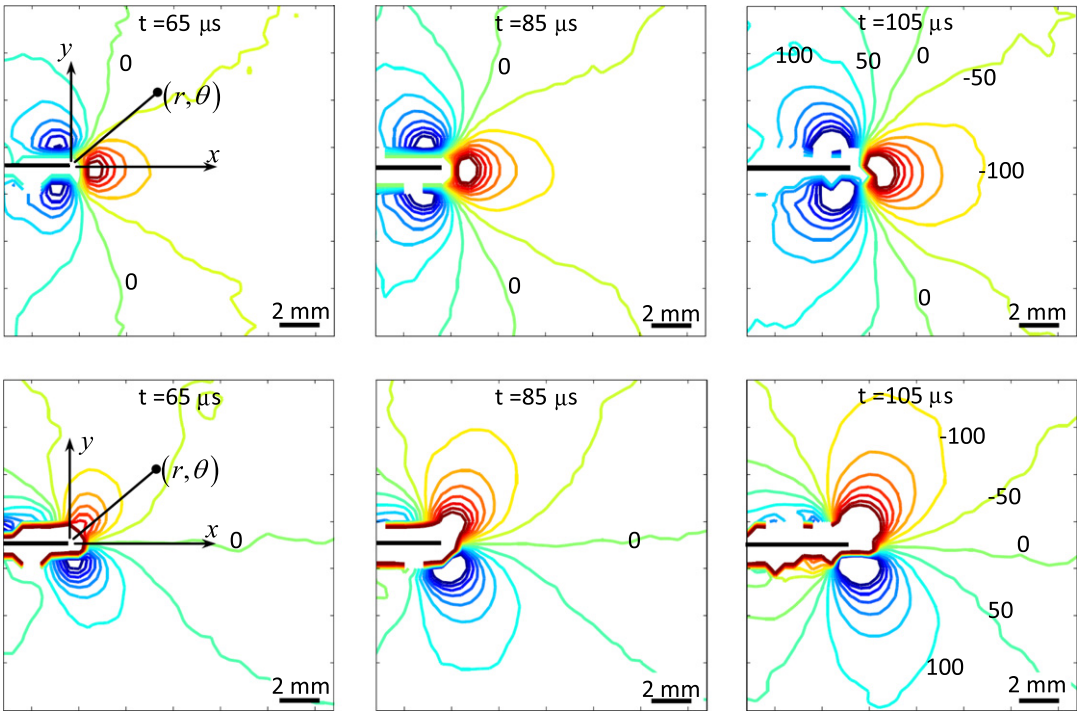

Fig. 8. Experimentally determined angular deflection (or, stress gradient) [ϕ_x(row 1) and ϕ_y (row 2)] contours near the crack tip at different instants of time after impact. Columns 1 and 2 correspond to a stationary crack, and column 3 to a growing crack. Contour interval is 50×10^{-5} radian.

nitude higher than the angular deflections that can be measured for commercial PMMA sheet of similar thickness [23,26]. As in case of the static crack problem, the boundary conditions such as symmetric stress gradients about the x-axis and asymmetric stress gradients in the y-direction relative to the x-axis, vanishing stress gradients away from the crack-tip were all utilized. Again, as noted earlier, image correlation operations introduce edge effects. This coupled with possible residual stresses (along the initial notch) and diffraction effects make contours not discernible in a narrow band along the two crack faces.

5.2. Extraction of K_I

The expressions for angular deflection fields corresponding to a steadily growing, straight crack are given by [18],

$$\phi_{x,y} = f(c; C_L, C_s) C_\sigma B \left[\left(-\frac{A_1}{2} \right) r^{\left(-\frac{3}{2}\right)} \begin{matrix} \cos \\ \sin \end{matrix} \left(-\frac{3\theta}{2} \right) \right] + HoT, \tag{14}$$

where f is a function of crack velocity, c, dilatational and shear wave speeds, C_L and C_S, respectively. In the above, HoT represents higher order terms of the asymptotic expansion for the angular deflection fields. Further, for plane stress conditions,

$$f(c; C_L, C_S) = \frac{(1+\alpha_S^2)(\alpha_L^2 - \alpha_S^2)}{4\alpha_S\alpha_L - (1+\alpha_S^2)^2} \tag{15}$$

where $\alpha_{L,S} = \sqrt{1 - \frac{c^2}{C_{L,S}^2}}$. The instantaneous crack velocity corresponding to each deformed image was calculated by measuring the change in crack length between successive images and dividing by the temporal separation between them. The post initiation crack velocities were in the 150–250 m/s range. (The dilatational and shear wave speeds were measured using ultrasonic pulse-echo measurements [28].) The angular deflection fields were then used with Eq. (14) to extract the dynamic mode-I stress intensity factor (K_I) history by performing overdeterministic least-squares analyses of measured data. As in the quasi-static case, data in the $(0.3 \leqslant r/B \leqslant 1.6)$ range were used in the regression analysis. For the dynamic analysis, $C_\sigma \approx -1.08 \times 10^{-10}$ m$^2/N$ was used in Eq. (14) based on the dynamic elasto-optic constant of PMMA reported in Ref. [15].

Fig. 9 shows the crack-tip K_I histories computed using the measured ϕ_x and ϕ_y fields. The error bars in Fig. 9 correspond to stress intensity factors obtained by using different subsets of the radial extent $(0.3 \leqslant r/B \leqslant 1.6)$ in the analysis. A monotonic increase in K_I prior to crack initiation can be seen. The crack initiation ($\sim$1.8 MPa $\sqrt{\text{m}}$) is signified by a noticeable dip in the history at approximately 90 μs after impact. Following crack initiation, again a monotonic increase in K_I seems to ensue over the next 50 μs time window.

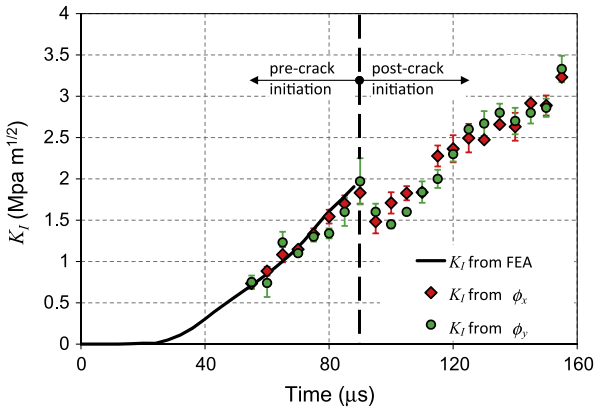

Fig. 9. Dynamic mode-I stress intensity factor histories from overdeterministic least-squares analysis of angular deflection data. Solid line is obtained from finite element analysis.

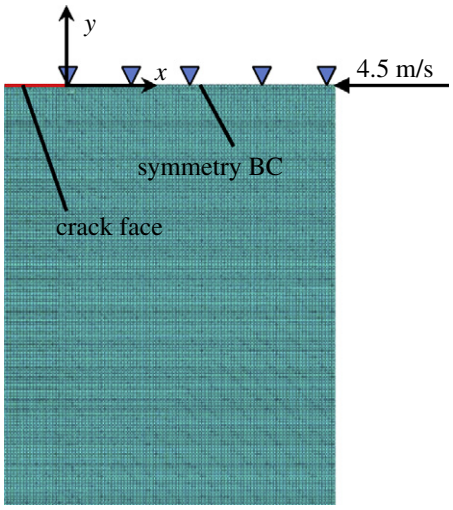

Fig. 10. One-half finite element model used for performing elasto-dynamic analysis.

Also included in Fig. 8 is the numerically determined K_I history up to crack initiation, represented as a solid line obtained, from a complementary finite element analysis. The finite element simulation was performed using ABAQUS™/Explicit software package that used one-half symmetric model of the experiment. The model was discretized into 29,979, four node bilinear plane stress quadrilateral elements with reduced integration and hour glass control. The time steps during the analysis were allowed to be automatically controlled by the explicit integration scheme. The dynamic elastic modulus and Poisson's ratio of PMMA used in the simulation were obtained from ultrasonic pulse-echo measurement of longitudinal and shear wave speeds [28] and mass density of PMMA. The measured plunger velocity of 4.5 m/s was used as an input in the simulation. The boundary conditions shown in Fig. 10 correspond to a half symmetric model of the dynamic crack experiment. The crack opening displacements (COD) along the crack face were extracted every 5 μs and the apparent mode I stress intensity factor $(K_I)_{app}$ computed using [15]

$$(K_I(t))_{app} = \frac{E\sqrt{2\pi}}{4\sqrt{r}} u_2(t); \quad (r, \theta = \pi) \tag{16}$$

where E = 5.8 GPa is the dynamic elastic modulus [26] of PMMA and u_2 is half COD of the crack flanks. By extrapolating the linear portion of the $(K_I)_{app}$ values plotted as a function of the radial distance r to the crack-tip, instantaneous (K_I) was determined. These simulations were limited to the case of a dynamically loaded stationary crack and hence the comparison of instantaneous K_I history from measurements and simulations are valid up to crack initiation. Accordingly, the numerical data from simulations are superposed on the experimentally extracted K_I values up to the observed crack initiation time. A good agreement between the two is evident, supporting the feasibility of DGS method for studying dynamic fracture problems.

6. Dynamic punch impact problem

6.1. Square punch-crack analogy

Material failure due to high strain-rate loading is often initiated by shear localization [29]. One such scenario can be realized experimentally when a plate specimen is impacted on its side/edge by a square/flat punch. This results in shear bands originating at the punch-tip if the impact is sufficiently severe. One way of characterizing dynamic failure in such a scenario is by evaluating dynamic stress intensity factor history at the punch-tip [30]. This idea exploits the analogy between the problem of a square punch loading the edge of a semi-infinite plate and the problem of two semi-infinite collinear edge cracks loaded in the far-field in compression [29,31], as shown in Fig. 11. In this work, a PMMA plate was subjected to a dynamically applied transient load by a flat punch, and the resulting angular deflection fields were measured using the DGS technique. Further, citing the punch-tip–crack-tip analogy, the analytical crack-tip angular deflection field equations were used to obtain the instantaneous stress intensity factor (K_P) histories at the punch-tip.

6.2. Experimental setup

The photograph of the experimental setup used for studying the punch-tip deformations caused by a dynamic transient loading by a square punch using DGS is shown in Fig. 12. The loading device consisted of an Al 7075-T6 long-bar (2 m long, 25.4 mm diameter), a gas-gun and the high-speed digital image acquisition system (the one used in the dynamic fracture experiment). The long-bar was aligned with the gas-gun barrel containing a 305 mm long, 25.4 mm diameter cylindrical striker also made of Al 7075-T6. Its leading head was machined flat, as shown in the inset in Fig. 12, so that it makes a square areal contact with the long-edge of the specimen. The specimen, a $160 \times 90 \times 5.7$ mm^3 clear PMMA plate, was placed on an adjustable platform and its long side was registered against the flat head of the long-bar as shown in Fig. 12. The loading was initiated by suddenly releasing the compressed air in the gas-gun cylinder using a solenoid valve to propel the striker towards the long-bar. The accelerating striker impacted the long-bar and initiated a compressive stress wave that traveled the length of the bar before imparting a transient punch-load to the edge of the specimen. An electrical circuit, closed when the striker contacted the long-bar, was used to trigger a delay generator which in turn activated the camera with a user-specified delay. A strain gage (CEA-13-062UW-350 from Vishay Micro-measurements) affixed to the long-bar, and connected to a LeCroy digital oscilloscope via an Ectron signal conditioner was used to measure the strain history $\varepsilon_I(t)$ (inset in Fig. 12) in the long-bar during the transient event [32].

The distance between the specimen and the camera lens (L) was ~1000 mm and the one between the specimen mid-plane and the target plane was (Δ) 28.2 mm. Using the high-speed camera, a set of 32 reference images, one for each sensor, were first captured under no-load condition at 200,000 frames per second. Next, the specimen was subjected to a dynamic load using the long-bar setup. During loading, a set of 32 consecutive images of the specimen undergoing deformation were captured in real-time at the same framing rate. The deformed–undeformed (reference) image pairs for each of the 32 CCD sensors were then correlated to obtain the in-plane displacement fields, δ_x and δ_y. As in the previous experiments, a facet/sub-image size of 15×15 pixels (1 pixel = 37 μm on the target plane) without any overlap was used during image analyses for extracting displacement components. The displacement fields were then used to compute the angular deflection fields (ϕ_x and ϕ_y), and are shown in Fig. 13 for three different time instants after the start of the transient loading event. (The time $t = 0$ corresponds to the instant at which the stress waves in the long bar reach the specimen edge.) The resulting angular deflection contours are plotted with a contour interval of 50×10^{-5} radians. The contour levels were assigned using the

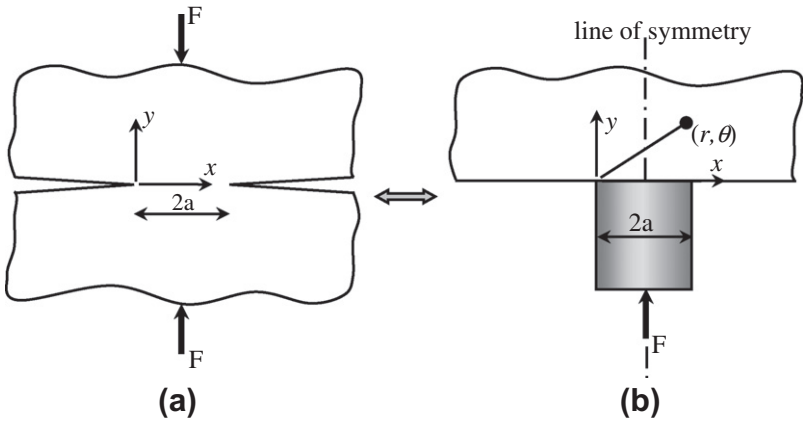

Fig. 11. Analogy between a compressively loaded collinear semi-infinite double crack in an infinite body (a) and punch loaded semi-infinite plate (b).

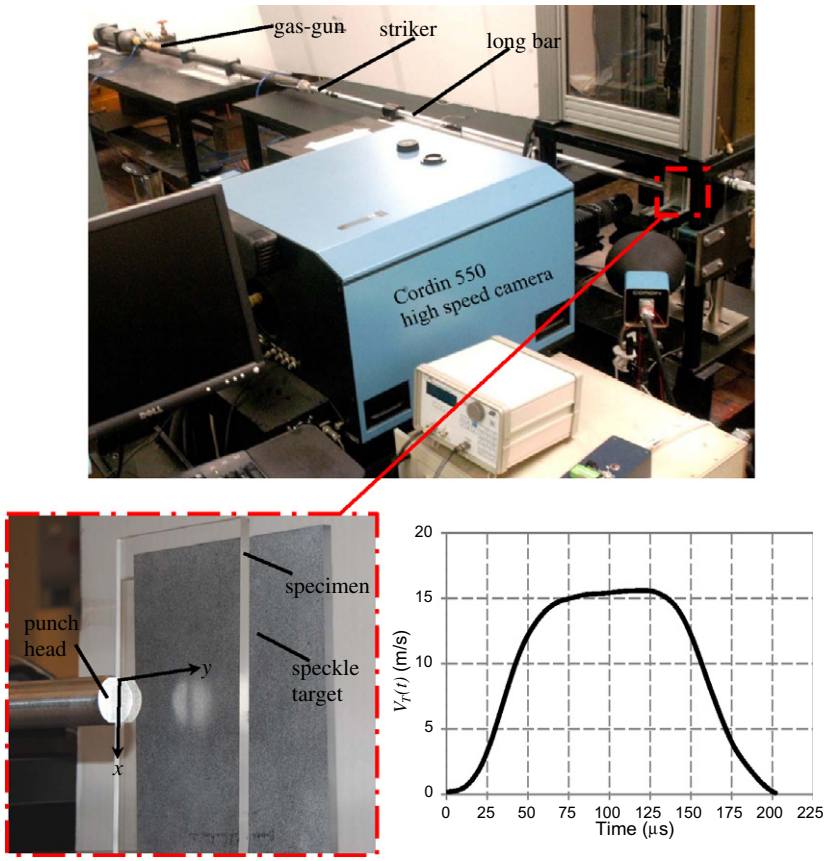

Fig. 12. Photograph of the experimental setup used to perform punch tip deformation field mapping using DGS (top), specimen close-up (bottom left), and transmitted particle velocity history from strain gage measurements in the long bar (bottom right).

boundary conditions, namely, symmetry about the loading axis, vanishing stress gradients away from the punch-tip, and also based on the punch–crack analogy.

6.3. Extraction of punch-tip stress intensity factors

In Fig. 13, it can be seen that the contours for ϕ_x above the x-axis qualitatively resemble the ϕ_x contours in Fig. 8 for a mode-I crack-tip. However, the resemblance of ϕ_y counterparts from the punch experiments with that of the mode-I crack experiments is less obvious. This difference is attributed to the compression dominated contact region ahead of the flat punch. This is also equivalent to the two interacting crack-tips depicted in the schematic for crack-tip–punch-tip analogy in Fig. 11. Nevertheless, the ϕ_x and ϕ_y contours obtained from the punch and the crack experiments show qualitative similarity in the $70^\circ \leqslant \theta \leqslant 180^\circ$ range. Accordingly, it was assumed that it is reasonable to use Eq. (14) to extract the punch-tip stress intensity factor, after replacing K_I with K_P as,

$$\phi_{x,y}(t) = C_\sigma B\left[\left(-\frac{K_P(t)}{2}\right)\sqrt{\frac{2}{\pi}}r^{\left(-\frac{3}{2}\right)}\begin{matrix}\cos\\ \sin\end{matrix}\left(-\frac{3\theta}{2}\right)\right], \tag{17}$$

in the mode-I crack-tip equations. (In the above equation, B = 5.7 mm is the thickness of the sample.) Using the above equations and the measured angular deflection field data in the $(0.3 \leqslant r/B \leqslant 1.6,\ 70^\circ \leqslant \theta \leqslant 160^\circ)$ range, the dynamic stress intensity factor (K_P) history at the punch corner was again computed by performing an overdeterministic least-squares analysis of measured data. The results are shown in Fig. 14. The error bars in the graph correspond to K_P values obtained using different subsets of data in the $(0.3 \leqslant r/B \leqslant 1.6,\ 70^\circ \leqslant \theta \leqslant 160^\circ)$ range. The rate of increase in K_P is initially shallow, in agreement with the slope of the loading curve (see inset in Fig. 13), after which it monotonically increases. The K_P histories from both the angular deflection fields follow a similar trend. When compared to the dynamic crack-tip stress intensity factors (Fig. 9), the magnitude of dynamic punch-tip stress intensity factors are substantially higher. For example, at 65 μs after the first non-zero stress intensity factor, the punch-tip counterpart registers a value nearly 4 times the magnitude of the crack-tip

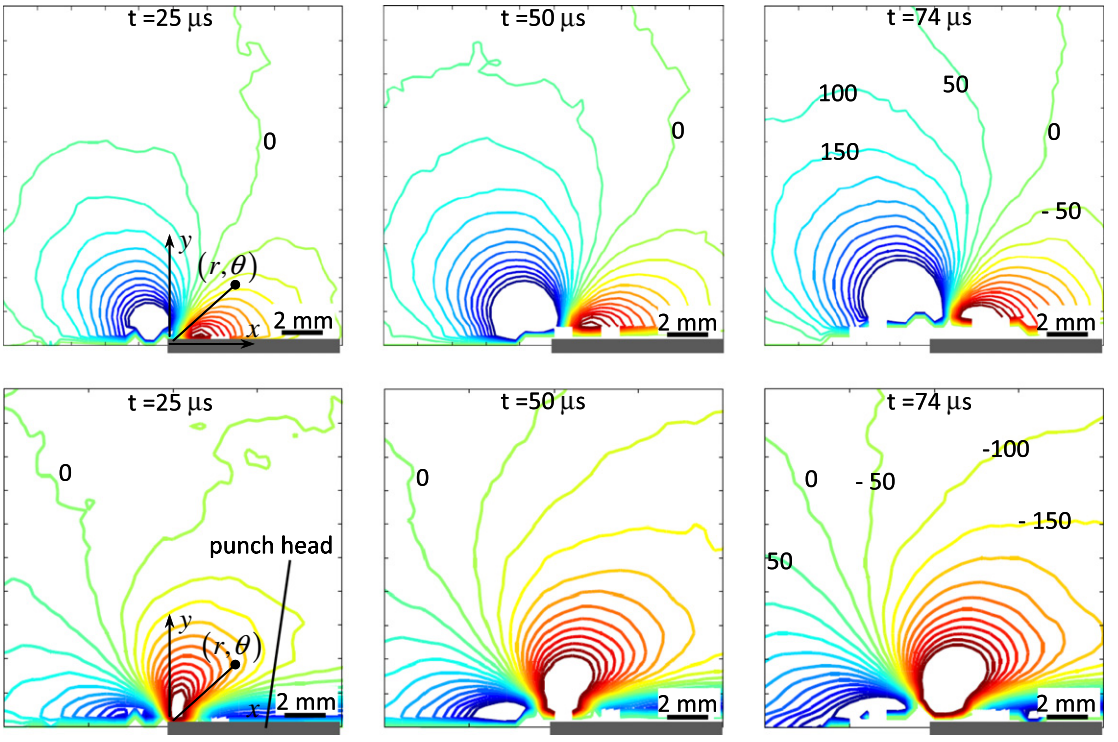

Fig. 13. Experimentally determined angular deflection (or stress gradient) [ϕ_x(row 1) and ϕ_y (row 2)] contours near a flat-punch tip. Contour interval is 50×10^{-5} radian.

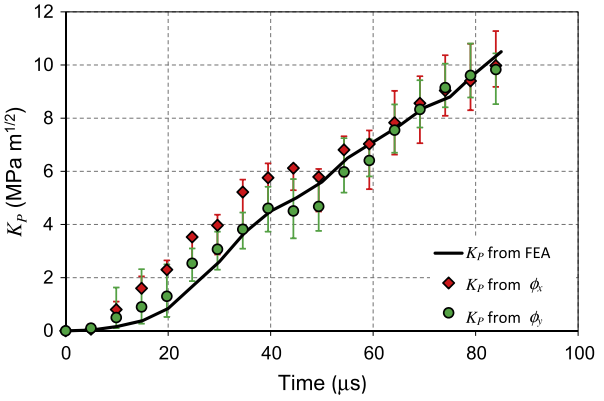

Fig. 14. Punch tip stress intensity factor histories (symbols) computed from measured stress gradient histories. Solid line represents finite element simulation results.

K_I. This is to be expected as the plate experiences compressive stress waves, unlike the dominant tensile stresses at the crack-tip.

The experiments were again numerically simulated via transient elasto-dynamic finite element analysis of the problem to provide a complementary set of results to the experimental measurements. The numerical simulation was performed using ABAQUS™/Explicit structural analysis software. The discretized numerical model along with the loading and boundary conditions used are shown in Fig. 15. It consisted of 33,574 four-node quadrilateral elements with the smallest element size ~ 0.5 mm. The time steps were allowed to be automatically chosen by the explicit integration scheme. The particle velocity (V_T) transmitted from the long-bar into the PMMA specimen was used as the input. The V_T history shown as an inset in Fig. 12 was calculated using [33],

$$V_T = V_I \frac{2\rho_I C_I A_I}{\rho_I C_I A_I + \rho_T C_T A_T}, \tag{18}$$

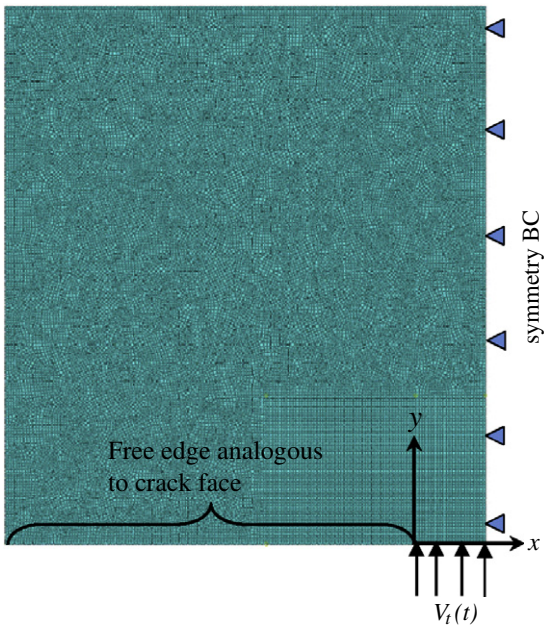

Fig. 15. Finite element model showing boundary conditions used to simulate the flat punch impact on the edge of PMMA plate.

Table 1
Material properties of long-bar and PMMA used in the dynamic flat punch experiments and numerical simulations.

Parameter	Value
Density of bar material (Al 7075-T6)	2730 kg/m^3
Longitudinal wave speed in bar	5200 m/s
Height of punch head	23.1 mm
Density of specimen material (PMMA)	1010 kg/m^3
Longitudinal wave speed in PMMA	2657 m/s

where $V_I = C_I\varepsilon_I$ is the particle velocity in the incident bar. The other parameters ρ, C, and A denote the mass density, bar wave speed and area, respectively, and subscripts I and T denote the incident and transmitted values. The measured material properties of the long-bar and PMMA are shown in Table 1. Analogous to the crack problem, instantaneous displacements (u_2) in the loading direction along the free edge of the impacted side of the PMMA sheet were extracted at 5 μs intervals. Using the method detailed earlier, these displacements were then used to extract the punch-corner stress intensity factor (K_P) using

$$K_P(t) = \frac{E\sqrt{2\pi}}{4\sqrt{r}}u_2(t); \quad (r, \theta = \pi). \tag{19}$$

The numerically obtained K_P history is plotted as a solid line in Fig. 14, which reveals a good agreement with the experimentally obtained values. This further substantiates the use of the punch–crack analogy.

7. Conclusions

A full-field optical metrology technique called Digital Gradient Sensing (DGS) method has been extended to study fracture and impact mechanics problems. The feasibility of the method to measure in-plane stress gradients in two orthogonal directions simultaneously in transparent objects is demonstrated. The method is based on the elasto-optic effect exhibited by materials subjected to non-uniform state of stress causing deflection of transmitted light rays. Digital image correlation method is employed to quantify angular deflections of light rays, which are then related to in-plane stress gradients under plane stress conditions.

The DGS method has been successfully implemented to measure the stress gradient fields around a crack-tip under both quasi-static and dynamic loading conditions. The quasi-static and dynamic stress intensity factors are computed by performing overdeterministic least-squares analysis on the measured optical data using prevailing crack-tip field equations. The evo-

lution of static and dynamic stress intensity factor histories are successfully compared with the ones obtained from analytical solutions and finite element simulations. In addition, a good full-field qualitative and quantitative agreement between the measured angular deflection values and the analytical solutions is also seen.

Further, the problem of a flat punch impacting the edge of a planar sheet is experimentally studied and the stress gradient fields around the punch-tip are measured using DGS. Citing the analogy between the problem of a compressively loaded double edge crack problem and the square punch problem, the analytical crack-tip angular deflection field equations are used to extract the punch-tip stress intensity factor history from measured deformation fields. The results are again in good agreement with the numerically obtained punch-tip stress intensity factor history computed using the same analogy but extracted from the crack opening displacements.

Acknowledgments

Partial support for this research through Grants W911NF-08-1-0285, W911NF-12-1-0317 from the U.S. Army Research Office and NSF CMMI-1232821 from the National Science Foundation is gratefully acknowledged.

References

[1] Patel PJ, Gilde GA. Transparent armor materials: needs and requirements. Ceram Trans 2002;134:573–86.
[2] Wright SC, Fleck NA, Stronge WJ. Ballistic impact of polycarbonate – an experimental investigation. Int J Impact Engng 1993;13(1):1–20.
[3] Kobayashi AS, Mall S. Dynamic fracture toughness of homalite-100. Exp Mech 1978;18(1):11–8.
[4] Arakawa K, Mada T, Takahashi K. Experimental analysis of dynamic effects in brittle fracture of PMMA. In: Hwang W, Han KS, editors. Fracture and strength of solids, Parts 1 and 2 book series: key engineering materials, vol. 183, no. 1; 2000. p. 265–270.
[5] Curran DR, Shockey DA, Seaman L. Dynamic fracture criteria for a polycarbonate. J Appl Phys 1973;44(9):4025–38.
[6] Dally JW, Barker DB. Dynamic measurements of initiation toughness at high loading rates. Exp Mech 1988;28(3):298–303.
[7] Ravichandar K, Knauss WG. An experimental investigation into dynamic fracture: crack initiation and arrest. Int J Fract 1984;25:247–62.
[8] Bless S, Chen T. Impact damage in layered glass. Int J Fract 2010;162(1–2):151–8.
[9] Subhash G, Haney EJ. Analysis of interacting cracks due to sequential indentations on sapphire. Acta Mater 2011;59(9):3528–36.
[10] Xu LR, Rosakis AJ. Real-time experimental investigation of dynamic crack branching using high-speed optical diagnostics. Exp Tech 2003;27(2):23–6.
[11] Park H, Chen W. Experimental investigation on dynamic crack propagating perpendicularly through interface in glass. J Appl Mech Trans ASME 2011;78(5).
[12] Dally JW. Dynamic photo-elastic studies of fracture. Exp Mech 1979;19(10):349–61.
[13] Parameswaran V, Shukla A. Dynamic fracture of a functionally gradient material having discrete property variation. J Mater Sci 1998;33(13):3303–11.
[14] Lee J, Kokaly MT, Kobayashi AS. Dynamic ductile fracture of aluminum SEN specimens an experimental–numerical analysis. Int J Fract 1998;93:39–50.
[15] Beinert J, Kalthoff JF. In: Sih GC, editor. Mechanics of fracture, vol. 7. Nijhoff Publishers; 1981. p. 281–328.
[16] Zehnder AT, Rosakis AJ. A note on the measurement of K and J under small-scale yielding conditions using the method of caustics. Int J Fract 1986;30(3):R43–8.
[17] Tippur HV, Krishnaswamy S, Rosakis AJ. Optical mapping of crack tip deformations using the methods of transmission and reflection coherent gradient sensing – a study of crack tip K-dominance. Int J Fract 1991;52(2):91–117.
[18] Krishnaswamy S, Tippur HV, Rosakis AJ. Measurement of transient crack tip deformation fields using the method of coherent gradient sensing. J Mech Phys Solids 1992;40(2):339–72.
[19] Sutton MA, Orteu U, Schreier H. Image correlation for shape, motion and deformation measurements. Springer; 2009.
[20] Kirugulige MS, Tippur HV, Denney TS. Measurement of transient deformations using digital image correlation method and high-speed photography: application to dynamic fracture. Appl Opt 2007;46(22):5083–96.
[21] Kirugulige MS, Tippur HV. Measurement of surface deformations and fracture parameters for a mixed-mode crack driven by stress waves using image correlation technique and high-speed photography. Strain 2009;45(2):108–22.
[22] Reu PL, Miller TJ. The application of high-speed digital image correlation. J Strain Anal Engng Des 2008;43(8):673–88.
[23] Periasamy C, Tippur HV. A full-field digital gradient sensing method for evaluating stress gradients in transparent solids. Appl Opt 2012;51(12):2088–97.
[24] Dally JW, Riley WF. Experimental stress analysis. 4th ed. College House Enterprises; 2005.
[25] Xu L, Tippur HV, Rousseau CE. Measurement of contact stresses using real-time shearing interferometry. Opt Engng 1999;38(11):1932–7.
[26] Periasamy C, Tippur HV. Measurement of orthogonal stress gradients due to impact load on a transparent sheet using digital gradient sensing method. Exp Mech; in press. http://dx.doi.org/10.1007/s11340-012-9653-x.
[27] Janssen M, Zuidema J, Wanhill RJH. Fracture mechanics. 2nd ed. VSSD; 2006.
[28] Butcher RJ, Rousseau CE, Tippur HV. A functionally graded particulate composite: preparation, measurements and failure analysis. Acta Mater 1998;47(1):259–68.
[29] Roessig KM, Mason JJ. Dynamic stress intensity factors in a two dimensional punch test. Engng Fract Mech 1998;60(4):421–35.
[30] Chen L, Batra RC. Material instability criterion near a notch-tip under locally adiabatic deformations of thermoviscoplastic materials. Theoret Appl Fract Mech 1998;30:153–8.
[31] Rubio-Gonzalez C, Mason JJ. Experimental investigation of dynamic punch tests on isotropic and composite materials. Exp Mech 1999;41(2):129–39.
[32] Periasamy C, Jhaver R, Tippur HV. Quasi-static and dynamic compression response of a lightweight interpenetrating phase composite foam. Mater Sci Engng-A 2010;527(12):2845–56.
[33] Meyers M. Dynamic behavior of materials. John Wiley & Sons, Inc.; 1994. p. 305–307.